CORA Cork Open Research Archive
Cartlann Taighde Oscailte Chorcaí

Title	NiVO3 fused oxide nanoparticles - an electrochemically stable intercalation anode material for lithium ion batteries
Authors	McNulty, David;Collins, Gillian;O'Dwyer, Colm
Publication date	2018-08-28
Original Citation	McNulty, D., Collins, G. and O'Dwyer, C. (2018) 'NiVO3 fused oxide nanoparticles - an electrochemically stable intercalation anode material for lithium ion batteries', Journal of Materials Chemistry A. doi:10.1039/C8TA05327H
Type of publication	Article (peer-reviewed)
Link to publisher's version	10.1039/C8TA05327H
Rights	© 2018, the Authors. Published by the Royal Society of Chemistry. All rights reserved. This is the Accepted Manuscript of an article published in Journal of Materials Chemistry A on 28th August, 2018, available online: https://dx.doi.org/10.1039/C8TA05327H
Download date	2026-11-05 18:41:46
Item downloaded from	https://hdl.handle.net/10468/6747

UCC
University College Cork, Ireland
Coláiste na hOllscoile Corcaigh

Electronic Supplementary Material (ESI) for Journal of Materials Chemistry A.
This journal is © The Royal Society of Chemistry 2018

Supporting Information for:

$NiVO_3$ Fused Oxide Nanoparticles – An Electrochemically Stable Intercalation Anode Material for Lithium Ion Batteries

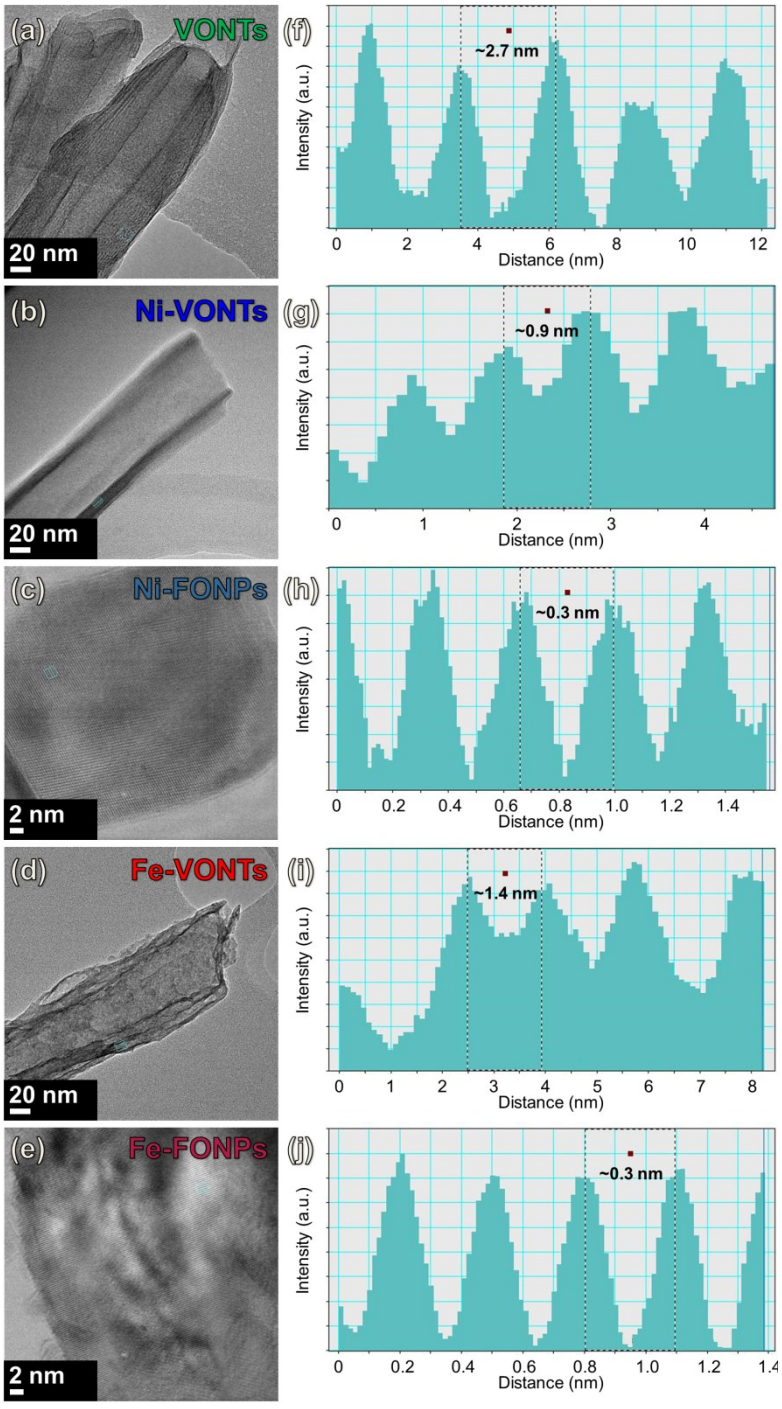


Fig. S1. TEM images of (a) as-prepared VONTs, (b) Ni-VONTs, (c) Ni-FONPs, (d) Fe-VONTs and (e) Fe-FONPs. Lattice spacings measured from TEM images using digital micrograph software for and (f) as-prepared VONTs, (g) Ni-VONTs, (h) Ni-FONPs, (i) Fe-VONTs and (j) Fe-FONPs.

X-ray diffraction patterns for $NiVO_3$ phase are confirmed as the phase of the Ni-FONPS. Both $NiVO_3$ and a related triclinic $CoVO_3$ phase show very good agreement with the experimentally acquired pattern for Ni-FONPs. Relative intensity differences from certain planes exist likely between the nanoscale nature of the FONPs compared to the bulk crystal analysed in the original $NiVO_3$ studies, that were limited to ~56 degrees double angle. We find no other patterns that closely match the pattern apart from $NiVO_3$, including other nickel vanadates such as $Ni_3V_2O_8$ (JCPDS 00-74-1484). We find no clear evidence that other isostructural compounds of different crystalline materials match the reference pattern, other than $NiVO_3$.

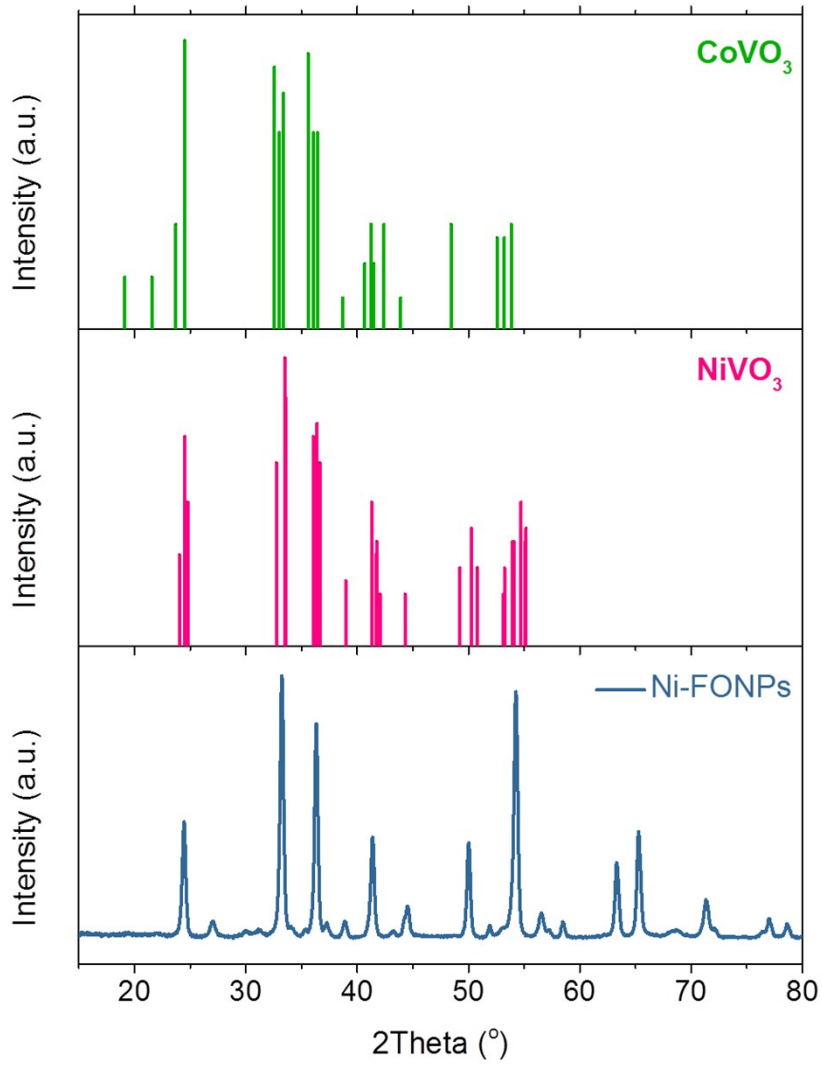


Fig. S2. XRD pattern for Ni-FONPs and reference stick patterns for $NiVO_3$ (JCPDS No. 00-027-1308) and $CoVO_3$ (JCPDS No. 00-026-0496).

SEM images of the ion-exchanged VONTs and heat treated FONPs are shown in Fig. S3. The tubular morphology of the Ni-VONTs and Fe-VONTs can be clearly seen in Fig. S3a

and d. The morphologies of the heat treated Ni-FONPs and Fe-FONPs are shown in Fig. S3b and e, respectively. FONPs are comprised of beaded rods of fused nanoparticles as can be seen the SEM images. SEM images of Ni-FONPs and Fe-FONPs after 500 galvanostatic cycles, with an applied specific current of 200 mA/g are shown in Fig. S3c and f, respectively. Energy-dispersive X-ray spectroscopy (EDS) spectra for ion exchanged VONTs, as-prepared FONPs samples and FONP samples after 500 galvanostatic cycles were acquired over the areas shown in the SEM images in Fig. S3a-f. The presence of peaks attributed to the presence of Ni can be seen in the spectra for Ni-VONTs and Ni-FONPs, before and after cycling. The relative amounts of each element present in the samples are listed in Table 1.

Table S1. Atomic % of elements present from EDS measurements.

	Atomic %					
Element	Ni-VONTs	Ni-FONPs	Ni-FONPs after 500 cycles	Fe-VONTs	Fe-FONPs	Fe-FONPs after 500 cycles
V	27.93	24.74	12.60	25.24	26.95	6.38
O	54.48	43.88	56.87	49.41	41.93	56.94
Fe	-	-	-	14.43	19.45	5.40
Ni	5.95	19.75	3.83	-	-	-
C	10.06	11.63	18.55	9.78	11.67	20.94
Cl	1.58	-	0.29	1.14	-	1.18
Si	-	-	0.34	-	-	0.40
P	-	-	1.45	-	-	1.01
F	-	-	6.07	-	-	7.75

The spectra for the Fe-VONTs and Fe-FONPs confirm the presence of Fe, V, O and C within the structure. The characteristic C peak at ~ 0.27 keV is likely due to presence of the hydrocarbon chain of any amine molecules remaining after the ion exchange reaction in the case of the Ni and Fe-VONTs and the thermal decomposition of amines in the case of the FONP samples, as well as adventitious carbon on the surface of the nanostructures. A low

intensity peaks associated with Cl is present due to Cl based precursors which were used as a source of both Fe and Ni ions. However, traces of Cl were not observed in the EDS spectra for the heated FONP samples.

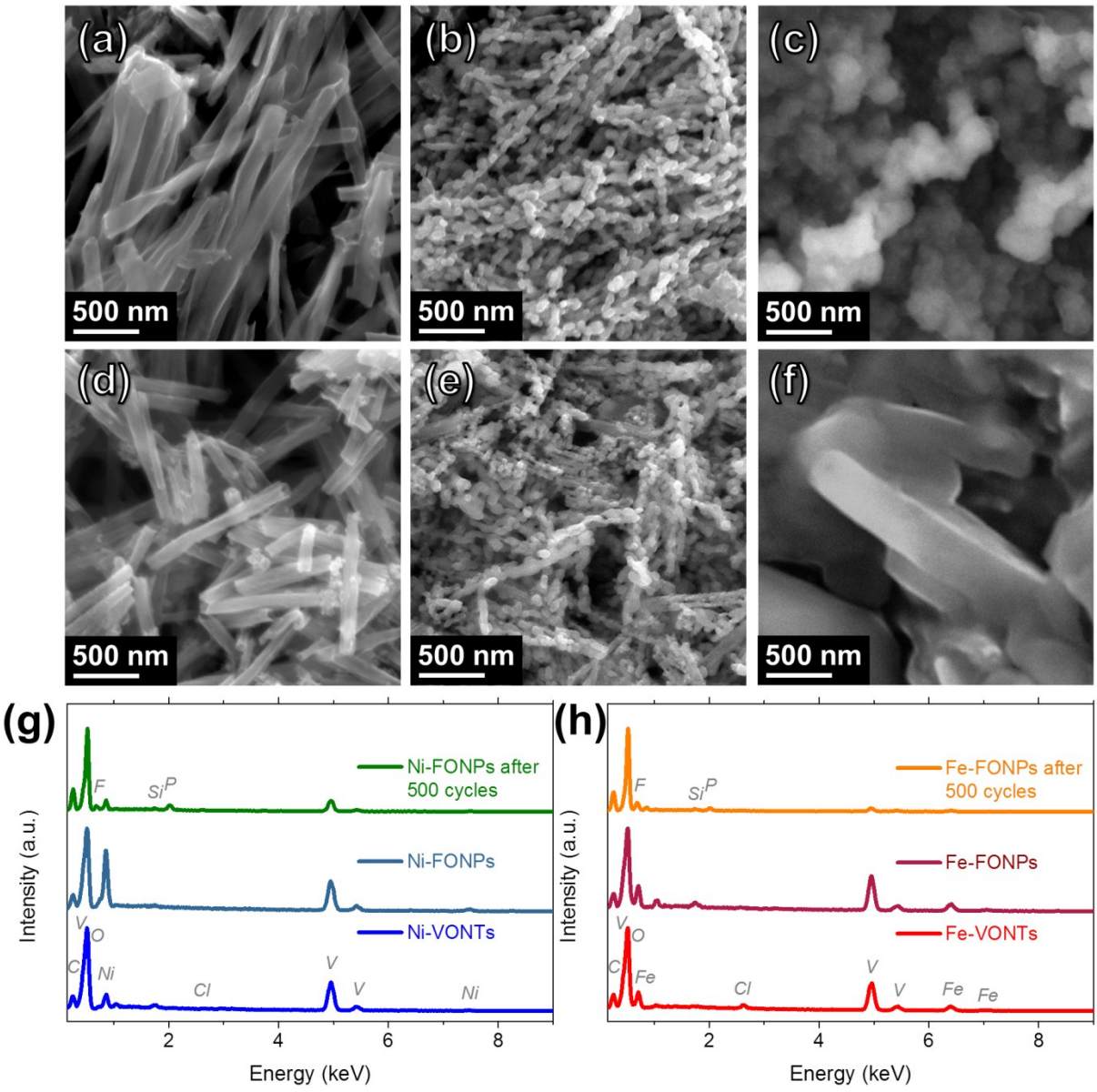


Fig. S3. SEM images of (a) Ni-VONTs, (b) Ni-FONPs, (c) Fe-VONTs and (d) Fe-FONPs. (e) EDS spectra for ion-exchanged VONT and heated FONP samples acquired from the areas shown in (a)-(d).

Ni and Fe-FONP samples after electrochemical testing contained traces of Si, P and F which were not observed in the spectra for the ion exchanged VONT samples or the FONP samples prior to electrochemical testing. The Si observed is due to the glass fibre separator which was used for all electrochemical tests, and P and F are present from the electrolyte

which was used (a 1 mol dm^{-3} solution of $LiPF_6$ in a 1:1 (v/v) mixture of ethylene carbonate in dimethyl carbonate with 3 wt% vinylene carbonate).

Elemental maps were acquired from scanning transmission electron microscope energy-dispersive X-ray spectroscopy in order to determine the distribution of each element present in Ni-FONPs and Fe-FONPs, as shown in Fig. S4. It can be seen from the elemental maps that Ni, V and O are homogeneously distributed within the Ni-FONPs. Likewise, Fe, V and O are also homogeneously distributed within the Fe-FONPs.

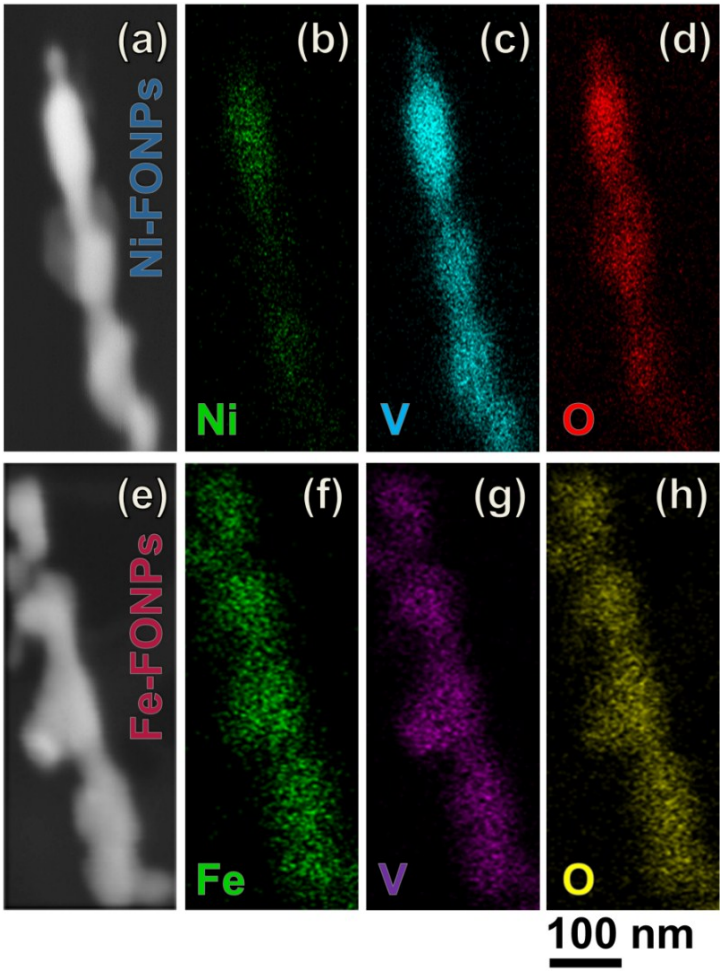


Fig. S4. Scanning transmission electron microscope (STEM) energy-dispersive X-ray spectroscopy (EDS) elemental maps for Ni-FONPs and Fe-FONPs illustrating the distribution of each element present.

Table S2. XPS binding energies for fitted peaks (in eV). The relative amounts of each vanadium oxidation state are shown in parentheses

	Fe 2p $_{3/2}$		Ni 2p $_{3/2}$		V 2p $_{3/2}$		
Sample	Fe^{3+}	Fe^{2+}	Ni^{3+}	Ni^{2+}	V^{5+}	V^{4+}	O 1s
Fe-VONTs	710.57 (37%)	712.19 (63%)	-	-	517.24 (91%)	515.77 (9%)	530.19
Fe-FONPs	710.89 (35%)	712.38 (65%)	-	-	517.30 (80%)	515.68 (20%)	530.11
Ni-VONTs	-	-	856.54 (72%)	855.75 (28%)	517.25 (88%)	515.82 (12%)	530.15
Ni-FONPs	-	-	857.43 (34%)	855.99 (66%)	517.27 (88%)	515.84 (12%)	530.17

The high resolution spectra for the O 1s region for all samples, contained three oxygen contributions, as shown in Fig. S5. The peak at ~ 530.2 eV is archetypal of metal-oxygen bonds. [1, 2] The peak at ~ 531.4 eV can be assigned to defects and a number of surface species including hydroxyls, chemisorbed oxygen or under-coordinated lattice oxygen. [3, 4] The peak present at ~ 533.3 eV can be attributed to multiplicity of physi- and chemisorbed water at or near the surface. [1, 2]

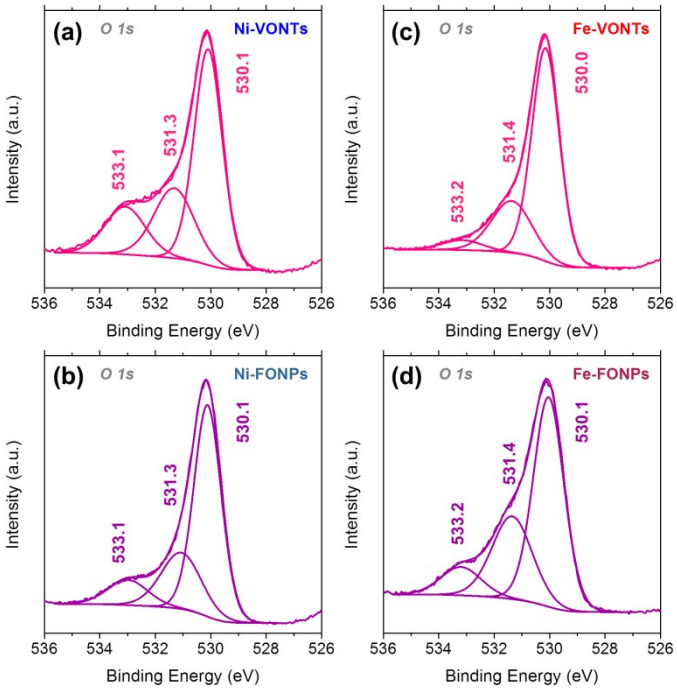


Fig. S5. XPS spectra of the O 1s regions for (a) Ni-VONTs, (b) Ni-FONPs, (c) Fe-VONTs and (d) Fe-FONPs

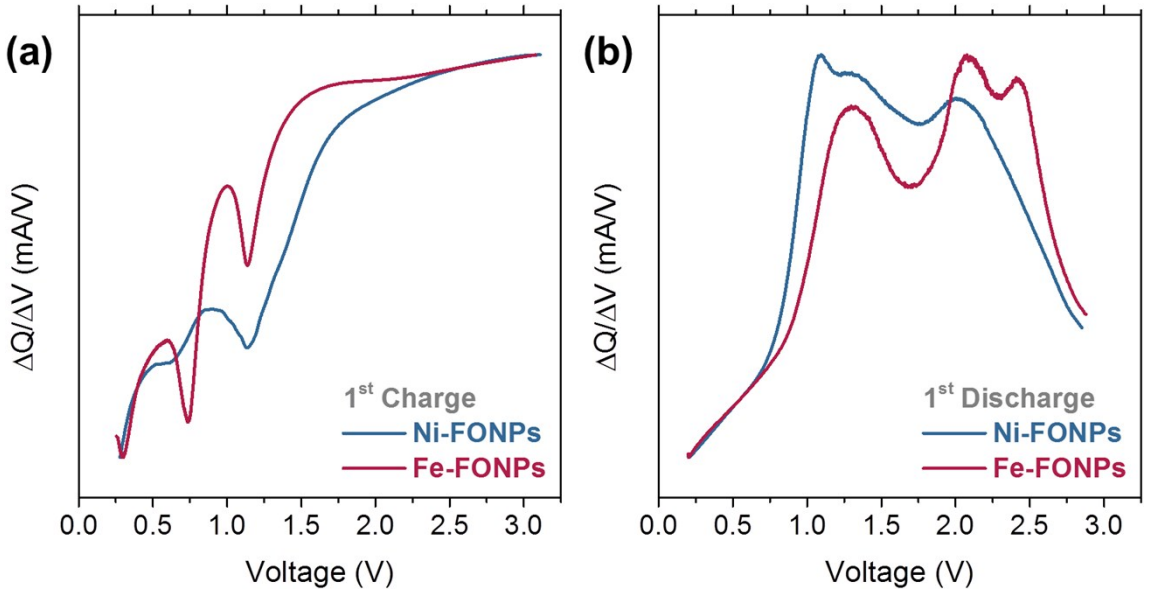


Fig. S6. Differential capacity plots calculated from (a) the first charge and (b) the first discharge voltage profiles for Ni-FONPs and Fe-FONPs, cycled galvanostatically using a specific current of 200 mA/g.

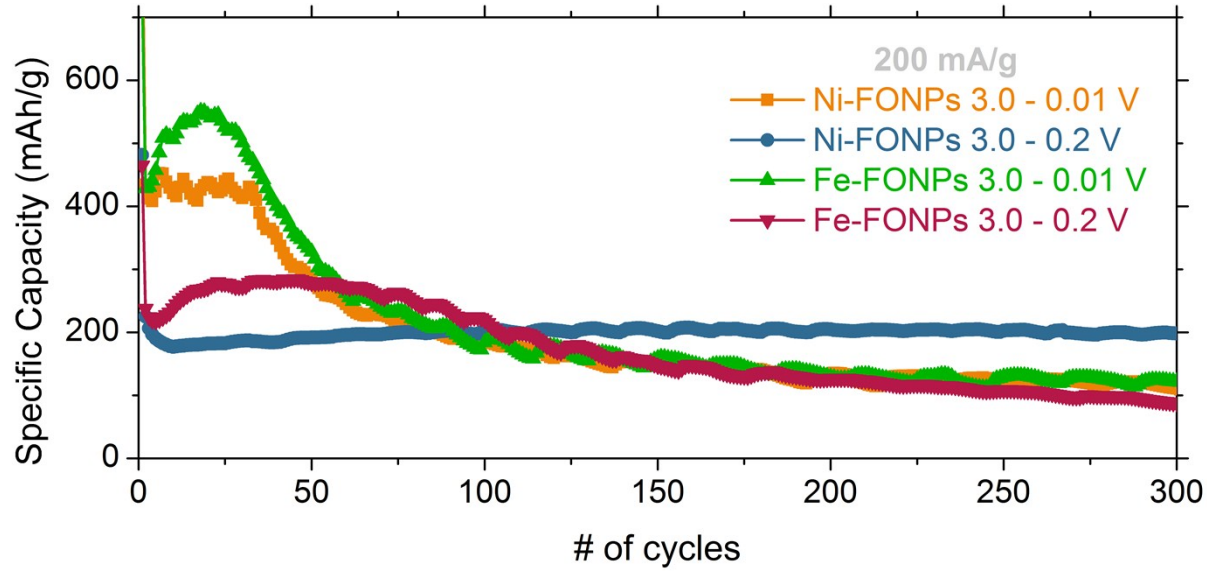


Fig. S7. Comparison of the specific capacity values obtained for Ni-FONPs and Fe-FONPs over 500 cycles in potential windows of 3.0 – 0.01 V and 3.0 – 0.2 V with an applied specific current of 200 mA/g.

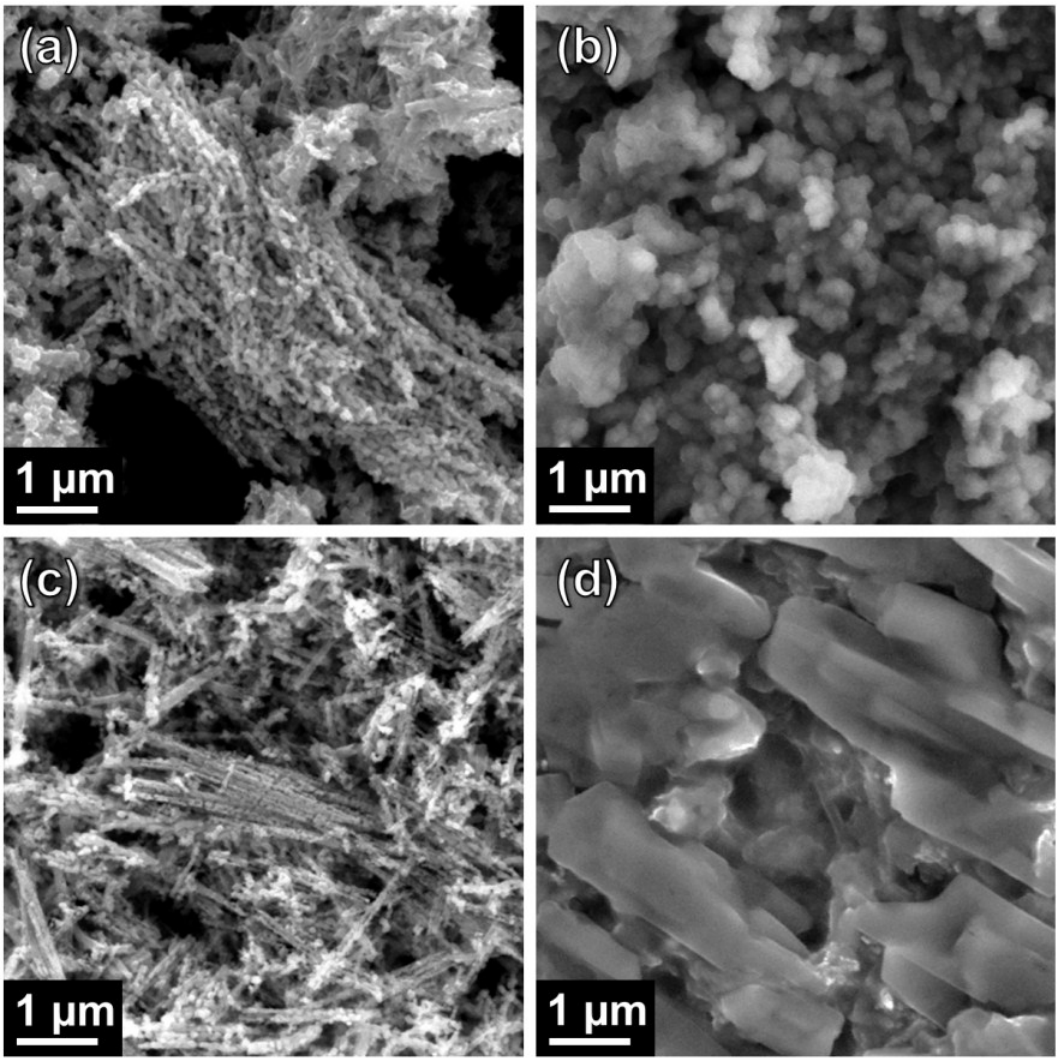


Fig. S8. SEM images of Ni-FONPs (a) before and (b) after 500 galvanostatic cycles and Fe-FONPs (c) before and (d) after 500 galvanostatic cycles using an applied specific current of 200 mA/g. The Fe_2O_3 and V_2O_3 nanocomposite material appears coated with the Li_2O phase, completely absent in the $NiVO_3$ cycled anode material. Note: All images were acquired at the same magnification (20,000×).

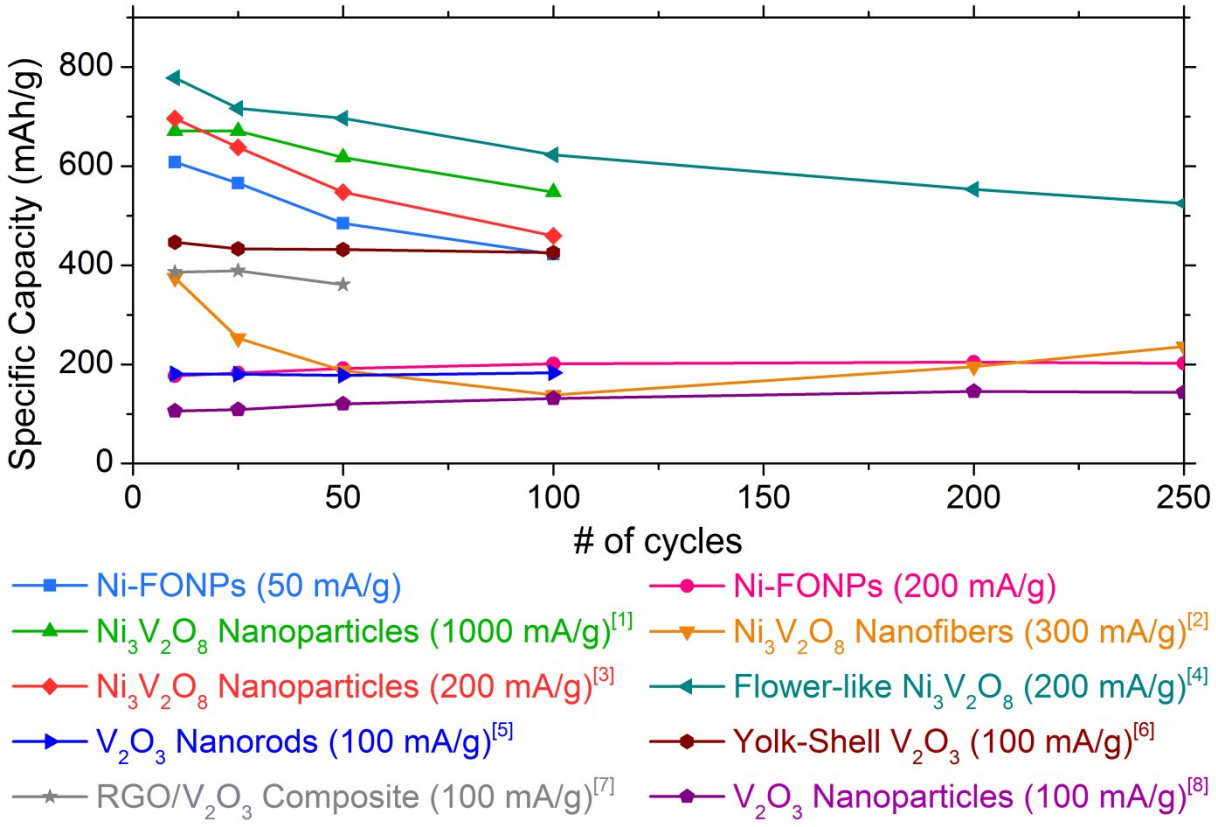


Fig. S9. Comparison of reported specific capacity values for $Ni_3V_2O_8$ and V_2O_3 nanostructures from the literature: $Ni_3V_2O_8$ nanoparticles[5], $Ni_3V_2O_8$ nanofibers[6], $Ni_3V_2O_8$ nanoparticles[7], flower-like $Ni_3V_2O_8$[8], V_2O_3 nanorods[9], yolk-shell V_2O_3[10], RGO/ V_2O_3 composite[11], V_2O_3 nanoparticles[12].

Table S3. Comparison of capacities obtained for various $Ni_3V_2O_8$ and V_2O_3 nanostructures from the literature

		Charge Capacity mAh/g						
Material	**C-rate**	**10th**	**25th**	**50th**	**100th**	**200th**	**250th**	**Ref.**
Ni-FONPs	50 mA/g	607.9	565.9	484.6	422.6	-	-	This work
Ni-FONPs	200 mA/g	177.2	182.7	191.8	201.3	204.7	202.5	This work
$Ni_3V_2O_8$ Nanoparticles	1000 mA/g	670.8	670.7	617.7	547.8	-	-	1
$Ni_3V_2O_8$ Nanofibers	300 mA/g	375.0	252.7	187.5	138.6	195.7	236.4	2
$Ni_3V_2O_8$ Nanoparticles	200 mA/g	696.4	638.0	547.4	459.7	-	-	3
Flower-like $Ni_3V_2O_8$	200 mA/g	778.2	716.9	696.5	622.9	553.4	524.8	4
V_2O_3 nanorods	100 mA/g	180.9	180.3	178.3	183.6	-	-	5
Yolk−Shell V_2O_3 Microspheres	100 mA/g	446.8	433.3	431.8	425.8	-	-	6
RGO/V_2O_3 Composite	100 mA/g	386.0	388.8	360.8	-	-	-	7
V_2O_3 nanoparticles	100 mA/g	106.2	109.2	120.3	131.4	145.5	143.6	8

References:

(1) Marco, J. F.; Gancedo, J. R.; Gracia, M.; Gautier, J. L.; Ríos, E.; Berry, F. J., Characterization of the Nickel Cobaltite, $NiCo_2O_4$, Prepared by Several Methods: An XRD, XANES, EXAFS, and XPS Study. *J. Solid State Chem.* **2000,** *153*, 74-81.

(2) Choudhury, T.; Saied, S. O.; Sullivan, J. L.; Abbot, A. M., Reduction of oxides of iron, cobalt, titanium and niobium by low-energy ion bombardment. *J. Phys. D* **1989,** *22*, 1185.

(3) Roginskaya, Y. E.; Morozova, O. V.; Lubnin, E. N.; Ulitina, Y. E.; Lopukhova, G. V.; Trasatti, S., Characterization of Bulk and Surface Composition of $Co_xNi_{1-x}O_y$ Mixed Oxides for Electrocatalysis. *Langmuir* **1997,** *13*, 4621-4627.

(4) Zhong, J.-H.; Wang, A.-L.; Li, G.-R.; Wang, J.-W.; Ou, Y.-N.; Tong, Y.-X., $Co_3O_4/Ni(OH)_2$ composite mesoporous nanosheet networks as a promising electrode for supercapacitor applications. *J. Mater. Chem.* **2012,** *22*, 5656-5665.

(5) Sambandam, B.; Soundharrajan, V.; Song, J.; Kim, S.; Jo, J.; Pham, D. T.; Kim, S.; Mathew, V.; Kim, K. H.; Sun, Y.-K.; Kim, J., $Ni_3V_2O_8$ nanoparticles as an excellent anode material for high-energy lithium-ion batteries. *J. Electroanal. Chem.* **2018,** *810*, 34-40.

(6) Lv, C.; Sun, J.; Chen, G.; Yan, C.; Chen, D., Achieving $Ni_3V_2O_8$ amorphous wire encapsulated in crystalline tube nanostructure as anode materials for lithium ion batteries. *Nano Energy* **2017,** *33*, 138-145.

(7) Soundharrajan, V.; Sambandam, B.; Song, J.; Kim, S.; Jo, J.; Pham, D. T.; Kim, S.; Mathew, V.; Kim, J., Bitter gourd-shaped $Ni_3V_2O_8$ anode developed by a one-pot metal-organic framework-combustion technique for advanced Li-ion batteries. *Ceramics International* **2017,** *43*, 13224-13232.

(8) Li, Y.; Kong, L.-B.; Liu, M.-C.; Zhang, W.-B.; Kang, L., One-step synthesis of micro/nano flower-like $Ni_3V_2O_8$ as anode for Li-ion batteries. *Mater. Lett.* **2017,** *186*, 289-292.

(9) Li, X.; Fu, J.; Pan, Z.; Su, J.; Xu, J.; Gao, B.; Peng, X.; Wang, L.; Zhang, X.; Chu, P. K., Peapod-like V_2O_3 Nanorods Encapsulated into Carbon as Binder-free and Flexible Electrodes in Lithium-ion Batteries. *J. Power Sources* **2016,** *331*, 58-66.

(10) Jiang, L.; Qu, Y.; Ren, Z.; Yu, P.; Zhao, D.; Zhou, W.; Wang, L.; Fu, H., In Situ Carbon-Coated Yolk–Shell V_2O_3 Microspheres for Lithium-Ion Batteries. *ACS Appl. Mater. Interfaces* **2015,** *7*, 1595-1601.

(11) Zhang, Y.; Pan, A.; Liang, S.; Chen, T.; Tang, Y.; Tan, X., Reduced graphene oxide modified V_2O_3 with enhanced performance for lithium-ion battery. *Mater. Lett.* **2014,** *137*, 174-177.

(12) Song, H. J.; Choi, M.; Kim, J.-C.; Park, S.; Lee, C. W.; Hong, S.-H.; Kim, D.-W., Li-electroactivity of thermally-reduced V_2O_3 nanoparticles. *Mater. Lett.* **2016,** *180*, 243-246.